Multiscale Damage Evolution Analysis of Aluminum Alloy Based on Defect Visualization

Yuquan Bao [1], Yali Yang [1,*], Hao Chen [1,*], Yongfang Li [1], Jie Shen [2] and Shuwei Yang [1]

1. School of Mechanical and Automotive Engineering, Shanghai University of Engineering Science, Shanghai 201620, China; m15221623776@163.com (Y.B.); liyongfang@sues.edu.cn (Y.L.); 18016334293@163.com (S.Y.)
2. College of Engineering and Computer Science, University of Michigan, Dearborn, MI 48128, USA; shen@umich.edu
* Correspondence: carolyn71@163.com (Y.Y.); pschenhao@163.com (H.C.); Tel.: +86-135-8590-1281 (Y.Y.); +86-135-8590-1312 (H.C.)

Featured Application: Life prediction for engineering materials.

Abstract: The evaluation of fatigue life through the mechanism of fatigue damage accumulation is still a challenging task in engineering structure failure analysis. A multiscale fatigue damage evolution model was proposed for describing both the mesoscopic voids propagation in the mesoscopic-scale and fatigue damage evolution process, reflecting the progressive degradation of metal components in the macro-scale. An effective method of defect classification was used to implement 3D reconstruction technology based on the MCT (micro-computed tomography) scanning damage data with ABAQUS subroutine. The effectiveness was validated through the comparison with the experimental data of fatigue damage accumulation. Our results indicated that the multiscale fatigue damage evolution model built a bridge between mesoscopic damage and macroscopic fracture, which not only used the damage variable in the macro-scale to characterize the mesoscopic damage evolution indirectly but also understood macroscopic material degradation behavior from mesoscale with sufficient precision. Furthermore, the multiscale fatigue damage evolution model could offer a new reasonable explanation of the effect of load sequence on fatigue life, and also could predict the fatigue life based on damage data by nondestructive testing techniques.

Keywords: multiscale; fatigue damage evolution; ABAQUS subroutine; 3D reconstruction; MCT scanning; fatigue life

1. Introduction

Fatigue fracture is one of the most common failure modes for engineering structures, and 80–90% of failures fall into this category [1–3]. Therefore, fatigue failure of metals has been the subject of study by many researchers. However, the understanding of fatigue mechanisms for evaluation of fatigue damage accumulation and fatigue life is still a challenging task up to now. With the development of theory and framework of the continuum damage mechanics (CDM), probably first presented by Kachanov [4], and the advance in technique for micro-observation of interior structure of steel materials, such as scanning electron microscopy [5], different methods and theories have been employed to study the evolution law of fatigue damage processes, such as the number of cycle load to failure, dissipated energy, and degradation in mechanical properties [6–16]. In recent years, more and more scholars have devoted to the study of fatigue damage processes.

On the one hand, many researchers pay attention to the continuous average damage variable to describe the degradation of material on a larger macro-scale, which is easy for engineering applications

due to its simplicity and effectiveness. Since Miner expressed this concept in the description of fatigue damage accumulation in 1945 [17], the cumulative fatigue damage theories have been developed increasingly, including the works of Marco and Starkey [18], Henry [19], Gatts [20], Manson [21], Chaboche [22], and many others. As a result, many different fatigue damage models have been developed based on the concept of CDM developed by Chaboche, Manson [23], Franke [24], and many others. However, most of the methods for macroscopic fracture are short for a deep and comprehensive understanding of microscopic damage mechanics theory in the study of the macro-scale fatigue process.

On the other hand, the methods of microscopic fatigue analysis, which are used to describe the microscopic defects initiation and growth behavior, are studied by some researchers, e.g., Miller [25], Angelova [26], and Polák [27], among many others. McClintock [28] and Rice and Tracey [29] have studied the nucleation, growth, and coalescence of cylindrical and spherical voids related to the fracture theory. McDowell et al. [30] developed a micro-scale fatigue model, which was able to characterize the effect of many micro-structural entities (cracks, voids, grains, etc.) on high cycle fatigue response of metallic materials. Leuders et al. [31] used the computed tomography for detecting the distribution of voids in Ti–6Al–4V samples manufactured by selective laser melting. More recently, Hu [32] analyzed the fatigue crack growth process in the material by using synchrotron X-ray micro-computed tomography. However, such attempts providing insight into the fatigue damage process have built-in complexities, which require accurate and detailed knowledge of microstructural features.

Both of the above research methods are based on the study of fatigue damage evolution in a single macro-scale or microscale. On the macro-scale, using a macro-variable to describe the continuous average fatigue damage accumulation extent cannot be explained by the fatigue failure mechanisms viewed from a smaller microscale. Nevertheless, the micro-analysis of microscopic defect behavior, focusing on only a few single cracks or voids, cannot evaluate average fatigue damage extent in a larger macro-scale. It has long been regarded as a very important issue to establish the micro-macro relationship for the fatigue accumulation process because such a relationship can enhance our understanding of the fundamental nature of fatigue mechanisms, but it is still a challenging task up to now.

There are few scholars who have studied multiscale fatigue damage evolution process and models. For instance, Desmorat et al. [33] employed the Eshelby–Kröner scale transition law and used a double-scale model to describe the HCF (high-cycle fatigue) phenomenon in which damage occurred only at the microscopic scale. Wan et al. [34] considered the phenomenon of building orientations and porosity in the additive manufacture structures and used the micro-scale damage-evolution equation to describe the damage evolution process at the macroscopic scale. However, such attempts focused on exploring the evolution process of micro-defect size and neglected the influence of microscopic defect shape and position distribution on fatigue damage. There is a paucity of modeling methods and fatigue damage evolution analyses based on micro-defects visualization processing and 3D reconstruction, considering aspects of the real random uniform micro-structural morphology. In this regard, this paper aimed to create a multiscale damage evolution model by an efficient and simple defect classification method and 3D reconstruction technology based on MCT (micro-computed tomography) scanning data. Firstly, fatigue specimens at different loading stages were scanned by MCT technology. The defect information for fatigue specimens was graded and simplified by the defect classification method, considering not only the micro-defect size but also the shape and position distribution on fatigue damage via AVIZO (3D visualization software, September 2, 2016, FEI SAS, Mérignac, France) visual processing. Then, 3D reconstruction was carried out. An equivalent simplified model was established by the ABAQUS subroutine. This model provided an effective tool to build a bridge between mesoscopic damage and macroscopic fracture, using the damage variable in macro-scale to characterize the mesoscopic damage evolution indirectly. At the same time, the residual fatigue life for engineering structures under unknown loading times could be predicted easily through the microstructure by nondestructive detection based on this methodological study.

2. Experiment

2.1. Material and Specimen Preparation

The composition of 6061-T6 aluminum alloy, which was used to manufacture test specimens, is shown in Table 1.

Table 1. Composition of 6061-T6 aluminum alloy.

Chemical Composition	Cu	Si	Fe	Mn	Mg	Zn	Cr	Ti	Other	AL
Ratio	25%	60%	70%	15%	85%	25%	16%	15%	15%	margin

The test pieces were prepared in accordance with the American Society for Testing Materials ASTM E8/E8M-15a standard and the metal material axial equal amplitude cyclic fatigue test method. While high-speed cutting is required, the alignment of the specimen should be ensured. The surface roughness was controlled by a polishing treatment. The specimen designed in this paper is shown in Figure 1.

| (a) | (b) |
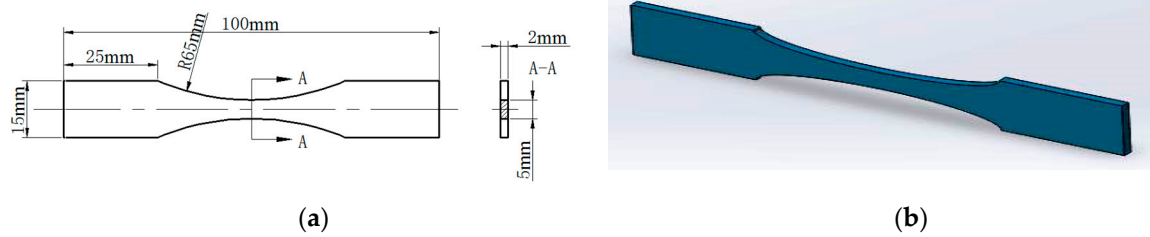
Figure 1. Specimens (**a**) Two-dimensions size of the specimens. (**b**) Three-dimensional view of the specimens.

2.2. Fatigue Test Procedures

The servo-hydraulic testing machine MTS809 with the capability of 100 kN in axial load (Figure 2) was used to accomplish the fatigue test at room temperature. The constant amplitude fatigue experiments were conducted at a loading rate of 50 Hz with the stress ratios $R = 0.1$ ($R = \sigma_{\min}/\sigma_{\max}$) by using sinusoidal waveform control.

Figure 2. MTS (Systems Corporation) fatigue tensile testing machine.

In advance, a large number of tests had been conducted to determine the fatigue life of the specimens experimentally, ranging from 10,779 to 11,453 cycles at a loading frequency of 50 Hz and

stress ratios $R = 0.1$ ($R = \sigma_{min}/\sigma_{max}$) by using sinusoidal waveform control. To reduce accidental experimental errors, the fatigue test was divided into three groups, and each group consisted of 5 cyclic loading stages (20,000 loading cycles, 40,000 loading cycles, 60,000 loading cycles, 80,000 loading cycles, 100,000 loading cycles), which were based on the maximum number of cycles determined as 100,000 cycles. These 5 stages were conducted on the corresponding 5 samples in each group, as shown in Figure 3.
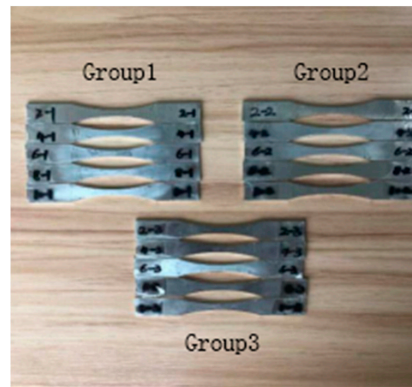
Figure 3. Test specimens.

## 3. Acquisition and Analysis of Defect Characteristics Information

3.1. Acquisition of Defect by X-ray Micro-Computed Tomography (MCT)

X-ray micro-computed tomography (MCT) (Vendor: Pheonix, AZ, USA), as a nondestructive technique, was used to get a quantitative estimate of mesoscopic voids in the damage specimens (Figure 4). In this process, an X-ray beam was focused on a particular region called the region of interest (ROI) of the specimen. ROI scan of the gauge length portion of the fatigue specimen could provide a deep insight into the shape and location distribution of voids, which is otherwise difficult to detect using any other conventional techniques, such as ultrasonic testing technology. A complete 360° scanning about the rotation axis of the specimen was carried out, and a total of 1600 images were taken. The exposure time for each image was 500 ms. The complete CT TIF section images of the ROI region were carried out by using Visual studio software from 2D data of each image. Four TIF diagrams selected randomly for specimen labeled 8-3 are shown in Figure 5; it would show different degrees of volume defects depending on perspectives.

**Figure 4.** X-ray micro-computed tomography system.
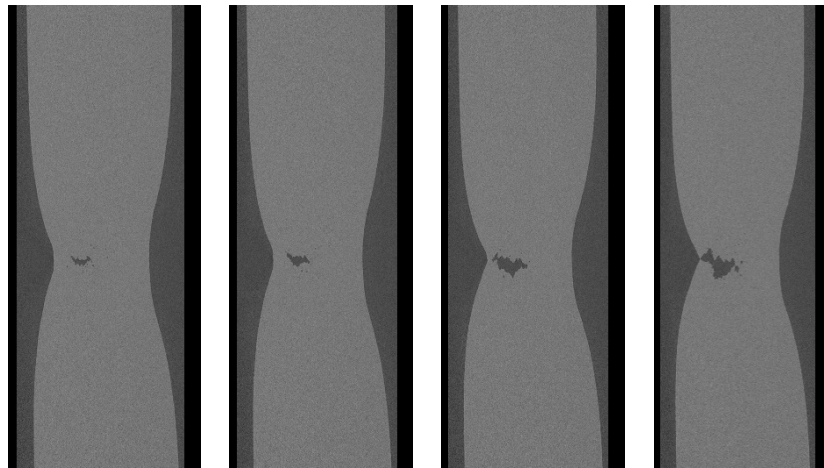
**Figure 5.** TIF slice diagram with different volume defects.

3.2. Visualization Processing of Defects Based on AVIZO

An effective visualization processing of slice data generated from CT was performed through importing TIF images with defect information into AVIZO, and the modular processing was conducted, as shown in Figure 6.
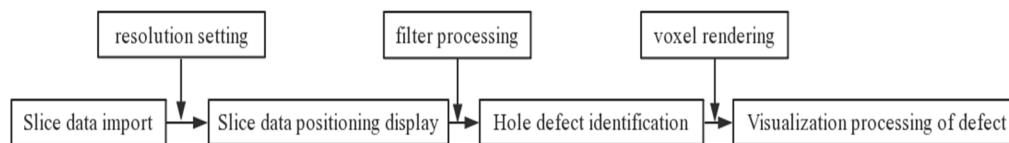

Figure 6. The flow chart of modular processing.

The resolution was set to 3 μm (CT scanning accuracy) in the process of importing TIF images into Avizo. The ortho-slice module was added to perform the TIF images data positioning explicit, as shown in Figure 7a. The non-local means filter module was used to filter the slice to remove the influence of the material itself on the hole defect recognition. The effect of TIF slice after noise removal is shown in Figure 7b. Comparing Figure 7a,b, it could be seen that the brightness of Figure 7b after noise removal was improved. The two-dimensional slice with noise removal was subjected to threshold segmentation through the interactive-threshold module to separate the matrix material from the void defect. The selection of the threshold was controlled during the segmentation process. If the threshold was too large, the matrix material would default to the void defect; and if the threshold was too small, the identified hole defect would be less than the actual number. Both of these situations were not conducive to subsequent defect analysis. The TIF diagram after segmentation and identification is shown in Figure 7c. The blue dot-like area in the figure indicates the void defect.

(a)　　　　　**(b)**　　　　　**(c)**
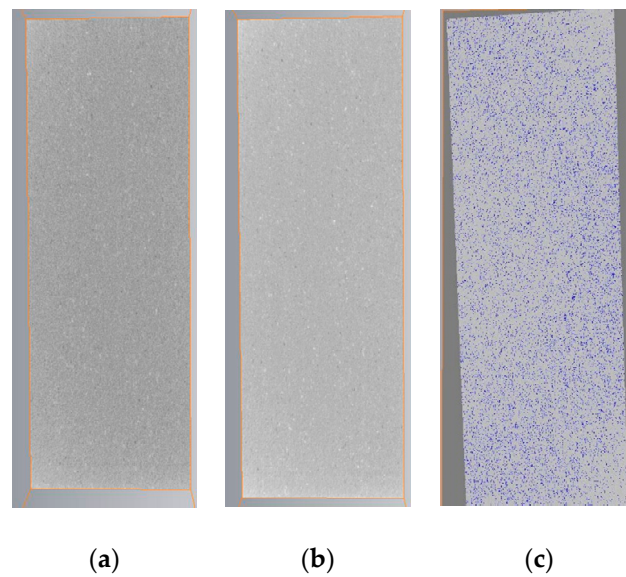
Figure 7. TIF diagram display. (**a**) TIF diagram after positioning display processing, (**b**) TIF diagram after noise filtering, (**c**) TIF diagram after threshold segmentation processing.

Moreover, voxel rendering was performed on the void defect by volume rendering, and the damage defect was three-dimensionally displayed and reconstructed to visually determine the position and degree of the damage. The 3D visualization of internal void defects for specimen labeled 8-3 is given in Figure 8.
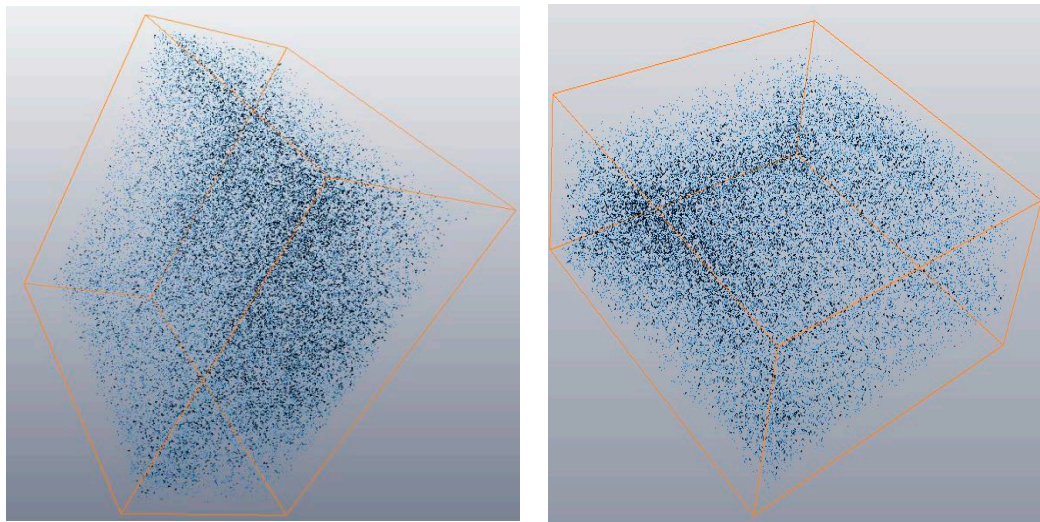
Figure 8. The 3D visualization of internal void defects for specimen labeled 8-3 from different perspectives.

3.3. Extraction and Analysis of Defect Characteristic Information

The characteristic information of defect (including void defect position, volume size, etc.) was obtained through the label analysis module for each cycle stage 3D model. Table 2 shows characteristic statistics of damage defects in different cycles.

Table 2. Characteristic statistics of damage defects in a different cycle.

Load Sequence (×10⁴)	Stage	2	4	6	8	10
Total number of voids (n)	Group1	35,106	215,398	125,703	35,684	20,982
	Group2	36,061	233,821	104,895	30,569	16,456
	Group3	34,854	190,636	76,695	24,534	18,672
The volume of maximum void (μm³)	Group1	972	1810	1970	3210	5671
	Group2	1190	2161	2275	3841	5319
	Group3	1021	2013	2144	3511	4782
Maximum damage surface area (μm²)	Group1	0.0022	0.0392	0.0345	0.0596	0.24
	Group2	0.0151	0.0275	0.0226	0.0459	0.197
	Group3	0.0073	0.0157	0.0553	0.0412	0.211
Porosity (%)	Group1	0.0004	0.0046	0.0031	0.0287	0.2421
	Group2	0.0009	0.0025	0.0673	0.0562	0.3866
	Group3	0.0006	0.0051	0.0242	0.0901	0.5293

The variation of the defect characterization with the different loading stages is illustrated in Figure 9. Figure 9a shows that the number of voids increased first to the peak and then decreased rapidly. Figure 9b–d is plotted for the variation of the maximum void, maximum damage surface, and porosity with the number of cycles. It could be seen that the rate of damage growth was not obvious at the beginning loading stage; however, at the later stage of loading, the damage growth rate increased sharply with the growth and association of defects.

(a)

(b)

(c)

(d)
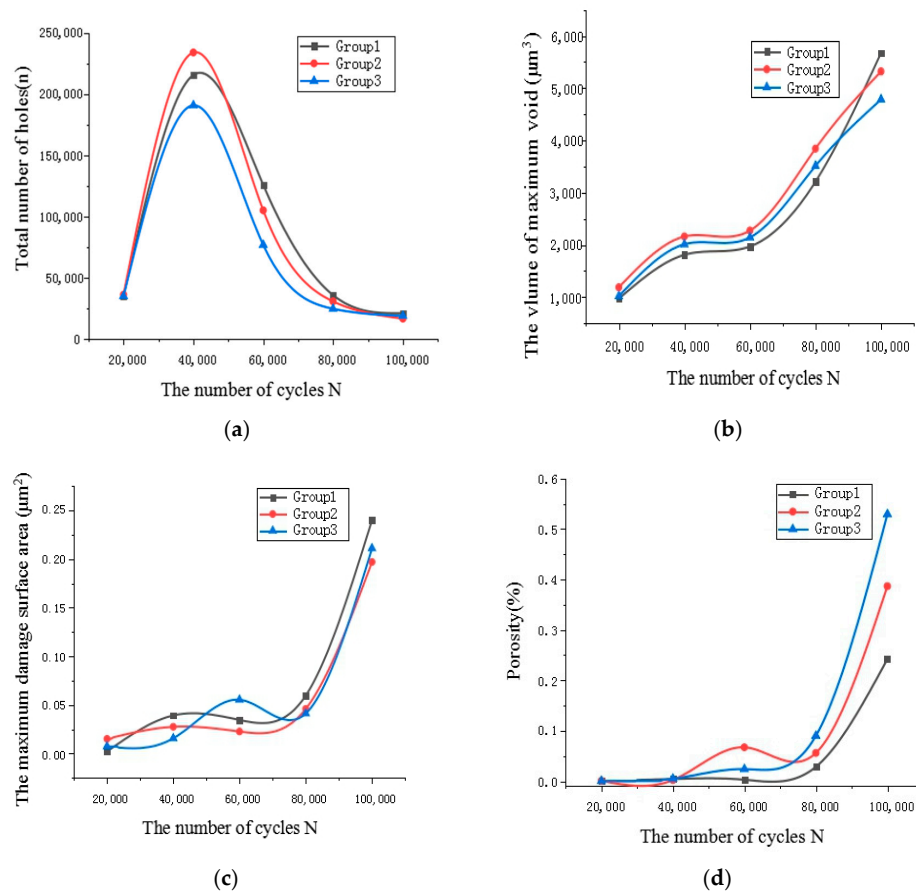
Figure 9. Variation of the voids damage characterization with the number of cycles N. (**a**) Variation of the total number of voids with the number of cycles N. (**b**) Variation of the volume of maximum void with the number of cycles N. (**c**) Variation of the maximum damage surface area with the number of cycles N. (**d**) Variation of the Porosity with the number of cycles N.

According to the variation of these damage characterizations (the number of hole defects, maximum hole, maximum damage surface, and porosity) with respect to the number of cycles, it could be concluded that the damage behavior mainly manifested that the initiation of void defects led to a slower growth of damage in the early loading stage. However, the growth rate of damage increased rapidly in the subsequent loading stages with the growth of micro-voids and the connection between adjacent voids.

The fatigue damage evolution process could be effectively characterized by the above damage parameters. Although some damage characterizations had volatility in the individual cycle stages, the overall tendency was consistent with the damage evolution law.

4. Damage Model

4.1. Establishment of an Equivalent Damage Model

It was difficult to conduct a damage evolution analysis and reduce the calculation time due to the shape and position of the plenty of mesoscopic defects inside the specimen. Therefore, a simplified equivalent multiscale damage model, which could reflect both mesoscopic damage and macroscopic fractures based on the grading of an internal defect, was established.

The equivalent mesoscopic void defects volume V_n and position information P_n were calculated based on original damage voids feature information. The volume of voids appeared in three orders of magnitude (10^{-6} mm^3, 10^{-7} mm^3, and 10^{-8} mm^3), which were, respectively, recorded as level 1, level 2, and level 3. The volume and position information of nth void for level 1 defects were recorded as V_{1n}, P_{1n}, and the remaining level 2 and level 3 were, respectively, recorded as V_{2m}, P_{2m} for m^{th} void and V_{3q}, P_{3q} for q^{th} void. The volume of the level 3 voids (10^{-8} mm^3) was averaged according to Equation (1) to obtain the average volume $\overline{V_3}$ since the volume of the level 3 voids was small. The level 1 voids were selected as base points, which were the main points with volume and location information; the level 2 and level 3 voids were selected as the reference points; the smallest volume in the level 3 voids was eliminated based on the effect of size on defect. Three levels (level 1, level 2, and level 3) of voids position information were placed in matrices P_1, P_2, and P_3, respectively. Matrix P_1 was a position matrix for the base points, and matrices P_2 and P_3 were recorded as the position matrices for the reference points, respectively, as shown in Equation (2).

$$\overline{V_3} = \frac{\sum\limits_{i=1}^{q} V_{3i}}{q} \tag{1}$$

$$P_1 = \begin{bmatrix} x_{11} & y_{11} & z_{11} \\ x_{12} & y_{12} & z_{12} \\ \vdots & \vdots & \vdots \\ x_{1n} & y_{1n} & z_{1n} \end{bmatrix} = \begin{bmatrix} p_{11} \\ p_{12} \\ \vdots \\ p_{1n} \end{bmatrix}, P_2 = \begin{bmatrix} x_{21} & y_{21} & z_{21} \\ x_{22} & y_{22} & z_{22} \\ \vdots & \vdots & \vdots \\ x_{2m} & y_{2m} & z_{2m} \end{bmatrix} = \begin{bmatrix} p_{21} \\ p_{22} \\ \vdots \\ p_{2m} \end{bmatrix}, P_3 = \begin{bmatrix} x_{31} & y_{31} & z_{31} \\ x_{32} & y_{32} & z_{32} \\ \vdots & \vdots & \vdots \\ x_{3q} & y_{3q} & z_{3q} \end{bmatrix} = \begin{bmatrix} p_{31} \\ p_{32} \\ \vdots \\ p_{3q} \end{bmatrix}, \tag{2}$$

$p_{1n} = \begin{bmatrix} x_{1n} & y_{1n} & z_{1n} \end{bmatrix}$ is a coordinate vector of the nth void of level 1, and $p_{2m} = \begin{bmatrix} x_{2m} & y_{2m} & z_{2m} \end{bmatrix}$ and $p_{3q} = \begin{bmatrix} x_{3q} & y_{3q} & z_{3q} \end{bmatrix}$ are the coordinate vector of the mth void of the level 2 and the qth void of the level 3, respectively. The MATLAB was applied to solve the aggregation

problem through the distance d between the reference points position vectors p_{2m}, p_{3q} and the base points position vector p_{1n}.

$$
\begin{aligned}
d_1^{(1)} &= \left| p_{11} - p_{21} \right| = \sqrt{(x_{11} - x_{21})^2 + (y_{11} - y_{21})^2 + (z_{11} - z_{21})^2}, \\
d_2^{(1)} &= \left| p_{11} - p_{22} \right| = \sqrt{(x_{11} - x_{22})^2 + (y_{11} - y_{22})^2 + (z_{11} - z_{22})^2}, \\
&\quad\vdots \\
d_m^{(1)} &= \left| p_{11} - p_{2m} \right| = \sqrt{(x_{11} - x_{2m})^2 + (y_{11} - y_{2m})^2 + (z_{11} - z_{2m})^2}, \\
d_{m+1}^{(1)} &= \left| p_{11} - p_{31} \right| = \sqrt{(x_{11} - x_{31})^2 + (y_{11} - y_{31})^2 + (z_{11} - z_{31})^2}, \\
&\quad\vdots \\
d_{m+q}^{(1)} &= \left| p_{11} - p_{3q} \right| = \sqrt{(x_{11} - x_{3q})^2 + (y_{11} - y_{3q})^2 + (z_{11} - z_{3q})^2},
\end{aligned}
\tag{3}
$$

From Equation (3), the distance between the first base point p_{11} and the remaining reference points could be obtained, and the result obtained was recorded as a vector D_1. Similarly, the distance from the nth base point to the remaining reference points could be calculated and recorded as a vector D_n, as shown in Equation (4).

$$
D = \begin{bmatrix} D_1 \\ D_2 \\ \vdots \\ D_n \end{bmatrix} = \begin{bmatrix} d_1^{(1)} & d_2^{(1)} & \cdots & d_{m+q}^{(1)} \\ d_1^{(2)} & d_2^{(2)} & \cdots & d_{m+q}^{(2)} \\ \vdots & \vdots & \cdots & \vdots \\ d_1^{(n)} & d_2^{(n)} & \cdots & d_{m+q}^{(n)} \end{bmatrix}
\tag{4}
$$

While the distance $d_o^{(n)}$ ($1 \le o \le m + q$ in matrix D was less than 3 mm, which was determined according to the simulation analysis by Digmat software, the volume information of the reference points with $d_o^{(n)}$ was retained and recorded as $V_{2r}^{(n)}$, $\overline{V_3^{(n)}}$. Where $V_{2r}^{(n)}$ is the rth volume of level 2 void, and $\overline{V_3^{(n)}}$ is the average volume of level 3 voids, respectively. In addition, Table 3 shows that the distance d between each pair of the base points was larger than 3 mm, eliminating the interaction between the base points. The effective voids volume V_n and position information P_n in the equivalent model were derived from Equations (5) and (6).

$$
V_n = V_{1n} + \sum_{i=1}^{r} V_{2i}^{(n)} + w\overline{V_3^{(n)}} \quad (1 \le r \le m , \ 1 \le w \le q)
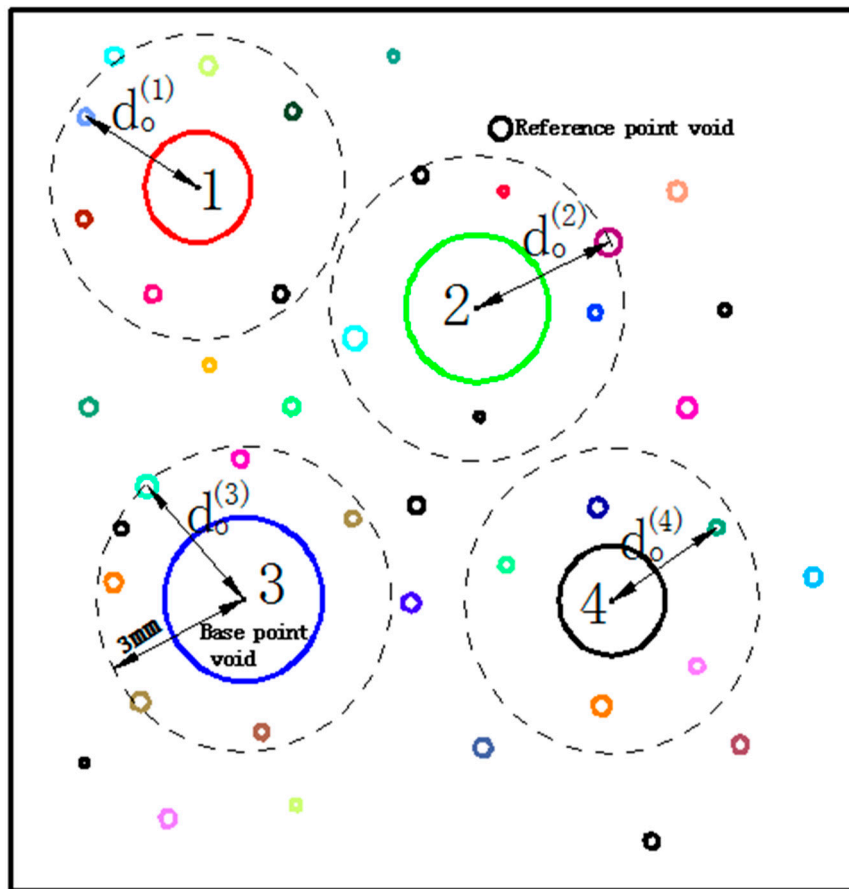\tag{5}
$$

$$
P_n = P_{1n}
\tag{6}
$$

Table 3. Distance d between each pair of base points.

Reference Point (n)	1	2	3	4	$\cdots$	n
1	0	3.6457	5.1247	4.2487	$\cdots$	3.8546
2	3.6457	0	4.2136	4.8712	$\cdots$	5.0147
3	5.1247	4.2136	0	3.0014	$\cdots$	3.2387
4	4.2478	4.8712	3.0014	0	$\cdots$	3.5601
$\vdots$	$\vdots$	$\vdots$	$\vdots$	$\vdots$	$\cdots$	$\vdots$
n	3.8546	5.0147	3.2387	3.5601	$\cdots$	0

The schematic diagram of the distance between the base point voids and the reference point voids is shown in Figure 10.


Figure 10. Schematic diagram of the distance between the base point voids and the reference point voids.

In addition, the voids defect was equivalent to a sphere model based on the simulation analysis by Digmat software. A lossless solid model was created by ABAQUS, and the equivalent position information P_n was assigned to the corresponding void defect model after the equivalent void model was created by the ABAQUS subroutine based on the equivalent void volume V_n. Then, the voids defect model assigned to the position information was moved to the corresponding position of the solid model by the ABAQUS subroutine and subjected to an ablation processing. Finally, the damage model with the equivalent void information was obtained. The schematic diagram of the equivalent damage model created by ABAQUS subroutine for specimen labeled 8-3 is demonstrated in Figure 11.
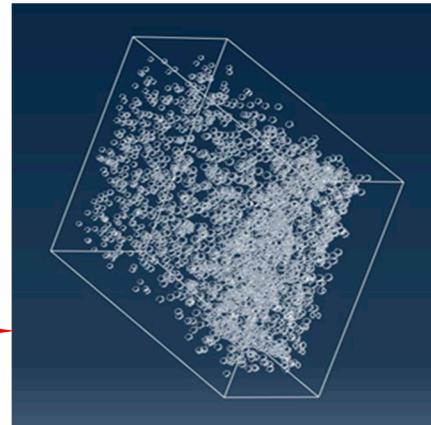
Damage model of the nth equivalent void

**(ABAQUS Subroutine)**
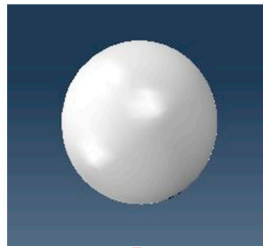
Position movement (ABAQUS Subroutine)
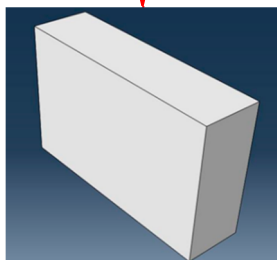
Ablation processing

**Damage model with equivalent voids**

Lossless solid model

Figure 11. Schematic diagram of the equivalent damage model created by ABAQUS subroutine for specimen labeled 8-3.

4.2. Fatigue Model Analysis and Validation

The equivalent multiscale damage evolution model was subjected to finite element tensile analysis by using displacement control in ABAQUS. The simulation results of the multiscale damage model of a fatigue specimen labeled 8-3 is shown in Figure 12. The effective Young's modulus E_{ds} obtained by the finite element analysis of the equivalent multiscale damage evolution model of three groups of fatigue specimens was fitted into a curve, as shown by the dotted line in Figure 13.

(**a**)　　　　　　　　　　　　　　　　　　　　(**b**)
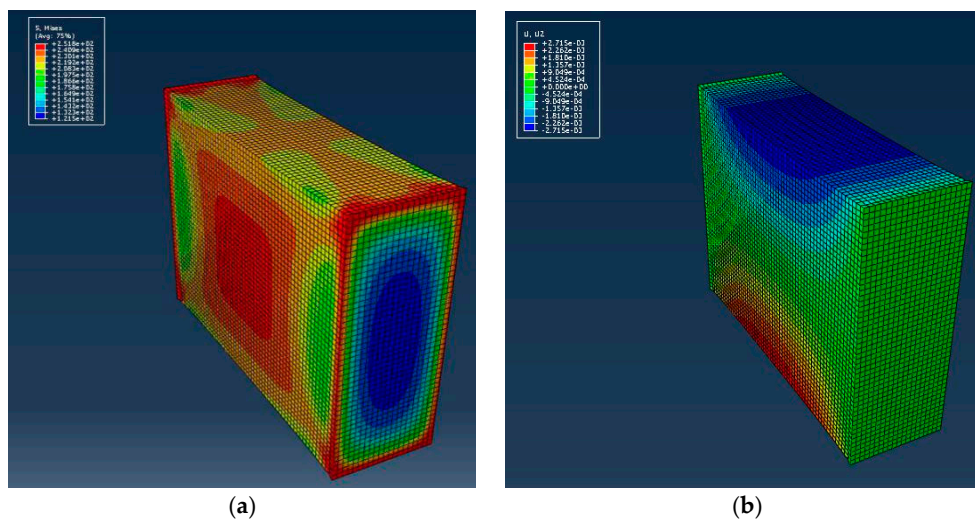
Figure 12. The tensile simulation results of damage model of specimens labeled 8-3. (**a**) Stress cloud map, (**b**) strain cloud map.
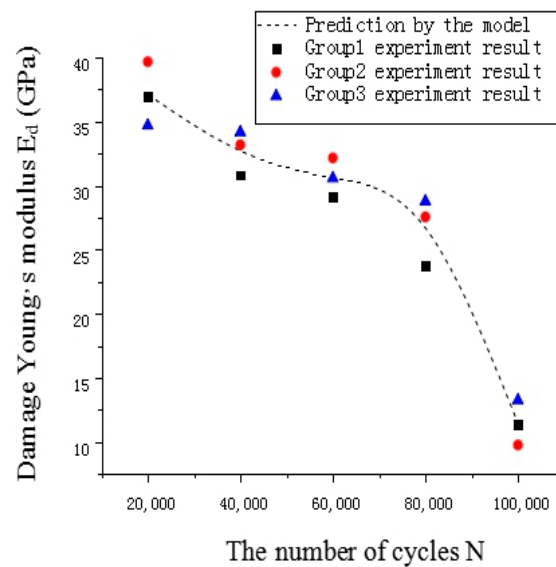
Figure 13. The verification of the fatigue damage evolution model.

In addition, the tensile experiments were conducted at a loading rate of 0.2 mm/min by using displacement control in electronic tensile testing machine to obtain damage Young's modulus E_{dt} of three groups of fatigue specimens. Table 4 shows the damage Young's modulus E_{dt} of three groups of fatigue specimens after the quasi-static tensile test.

Table 4. The Young's modulus E_{dt} of three groups of fatigue specimens after the tensile test.

load Sequence ($\times 10^4$)	Stage Group	2	4	6	8	10
Damage Young's modulus E_{dt} (GP$_a$)	Group1	36.581	31.816	29.109	24.169	11.356
	Group2	39.647	33.169	32.147	27.549	9.365
	Group3	34.946	34.149	30.564	28.764	13.248

In order to verify the proposed multiscale damage evolution model, the comparisons between the curve, predicted by the finite element numerical model parameters E_{ds}, obtained from ABAQUS and the tensile experimental results (Table 4) are shown in Figure 13. The comparisons showed that the fatigue damage evolution curves predicted by the multiscale damage evolution model agreed well with the experimental results, indicating that the proposed multiscale damage evolution model could describe not only macro-scale fatigue damage evolution process by using Young's modulus E but also describe the behavior of voids initiation and growth in mesoscopic scale. Therefore, the model built a bridge that used the effective Young's modulus E at the macro-scale to characterize the mesoscopic damage evolution.

5. Fatigue Life Prediction

Fatigue lives were predicted by establishing the relationship between the several important characteristic parameters: the damage Young's modulus E_d, the damage variable D, and the number of cycles.

By the continuous damage mechanism (CDM) [35,36] theory, the damage variable resulted from the initiation and growth of microvoids was often used to describe the degradation of material properties. For isotropic metal materials, the stiffness degradation represented by damage variable D is given by.

$$D = \frac{E - E_d}{E} \tag{7}$$

where E represents Young's modulus of material without damage, and E_d is the effective Young's modulus with damage.

The damage variable D of each loading stage was calculated by Equation (7) based on the effective Young's modulus E_d of each fatigue specimen after static tensile test in ABAQUS. Consequently, the relationship between damage parameter D and fatigue life in the fatigue process could be obtained. The variation of the damage variable D and the damage Young's modulus E_d with the number of loading cycles N is, respectively, plotted in Figure 14a,b.
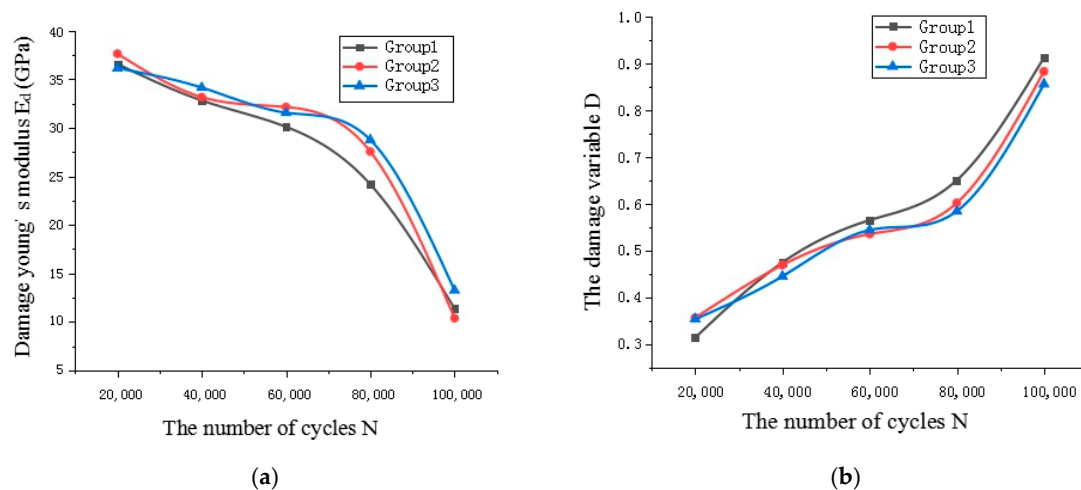
Figure 14. (**a**) Variation of Young's damage modulus E_d with the number of cycles N. (**b**) Variation of the damage variable D with the number of cycles N.

It could be seen from Figure 14a,b that the damage variable D increased with the increase of the number of loading cycles N, and the damage Young's modulus E_d decreased gradually. However, the damage Young's modulus E_d decreased drastically if the damage degree D exceeded 0.1, resulting in a sharp degradation of material properties. Moreover, Figure 14b shows that the damage parameter D of three groups of curves increased slowly in the early stage, which is the stable initiation stage of voids, and accounted for 10% to 80% of total life. After that, the damage parameter D increased rapidly in the unstable propagation stage of voids. However, no matter which damage stage the material was in, fatigue life could also be predicted conveniently based on the calculated damage variable D by the proposed multiscale damage evolution model for nondestructive detection.

6. Conclusions

The effectiveness of our multiscale damage evolution model was confirmed by using the experimental data of fatigue damage accumulation during the stages of voids initiation and growth. After that, the developed model was, respectively, applied to explain the effect of load sequence on fatigue life. In addition, the fatigue life of metal components and structures due to mesoscopic voids and growth and linkage was calculated from the damage variable D and the effective Young's modulus E_d at the macro-scale. According to the results of this study, the following conclusions could be presented:

(1) The proposed method of defect classification was effective to realize the three-dimensional reconstruction of the mesoscopic defects based on the mesoscopic defect data obtained by CT scanning technology.

(2) A new multiscale damage evolution model for fatigue damage accumulation had been developed, which built a bridge to describe the continuous average damage evolution process for metal fatigue components and structures in mesoscopic scale by macro damage variables for understanding metal fatigue failure mechanisms.

(3) The fatigue life was predicted with the damage data measured by nondestructive testing technology (CT scanning technology, etc.) based on the effectiveness of the multiscale damage evolution model.

References

1. Kaynak, C.; Ankara, A.; Baker, T.J. Effects of short cracks on fatigue life calculations. *Int. J. Fatigue* **1996**, *18*, 25–31. [CrossRef]
2. Lillbacka, R.; Johnson, E.; Ekh, M. A model for short crack propagation in polycrystalline materials. *Eng. Fract. Mech.* **2006**, *73*, 223–232. [CrossRef]
3. Cheung, M.S.; Li, W.C. Probabilistic fatigue and fracture analyses of steel bridges. *Struct. Saf.* **2003**, *23*, 245–262. [CrossRef]
4. Kachanov, L.M. Time of the rupture process under creep condition. *TVZ Akad. Nauk. Ssr Otd. Tech. Nauk.* **1958**, *8*, 26–31.
5. Pathan, A.K.; Bond, J.; Gaskin, R.E. Sample preparation for scanning electron microscopy of plant surfaces—Horses for courses. *Micron* **2008**, *39*, 1049–1061. [CrossRef]
6. Risitano, A.; Risitano, G. Cumulative damage evaluation of steel using infrared thermography. *Appl. Fract. Mech.* **2010**, *54*, 82–90. [CrossRef]
7. Fan, J.L.; Guo, X.L.; Wu, C.W.; Zhao, Y. Research on fatigue behavior evaluation and fatigue fracture mechanisms of cruciform welded joints. *Mater. Sci. Eng.* **2011**, *A528*, 8417–8427. [CrossRef]
8. Fan, J.L.; Guo, X.L.; Wu, C.W. A new application of the infrared thermography for fatigue evaluation and damage assessment. *Int. J. Fatigue* **2012**, *44*, 1–7. [CrossRef]
9. Belaadi, A.; Bezazi, A.; Bourchak, M.; Scarpa, F. Tensile static and fatigue behaviour of sisal fibres. *Mater. Des.* **2013**, *46*, 76–83. [CrossRef]
10. Zhou, Y.F.; Jerrams, S.; Chen, L. Multi-axial fatigue in magnetorheological elastomers using bubble inflation. *Mater. Des.* **2013**, *50*, 68–71. [CrossRef]
11. Azadi, M.; Farrahi, G.H.; Winter, G.; Eichlseder, W. Fatigue lifetime of AZ91 magnesium alloy subjected to cyclic thermal and mechanical loadings. *Mater. Des.* **2014**, *53*, 639–644. [CrossRef]
12. Moreno-Navarro, F.; Rubio-Gámez, M.C. Mean damage parameter for the characterization of fatigue cracking behavior in bituminous mixes. *Mater. Des.* **2014**, *54*, 748–754. [CrossRef]
13. Li, D.Z.; Han, L.; Thornton, M.; Shergold, M.; Williams, G. The influence of fatigue on the stiffness and remaining static strength of self-piercing riveted aluminium joints. *Mater. Des.* **2014**, *54*, 301–314. [CrossRef]
14. Shiri, S.; Pourgol-Mohammad, M.; Yazdani, M. Probabilistic Assessment of Fatigue Life in Fiber Reinforced Composites. In Proceedings of the ASME 2014 International Mechanical Engineering Congress and Exposition, Montreal, QC, Canada, 10–14 November 2014; p. V014T08A018.
15. Shiri, S.; Pourgol-Mohammad, M.; Yazdani, M. Effect of strength dispersion on fatigue life prediction of composites under two-stage loading. *Mater. Des.* **2015**, *65*, 1189–1195. [CrossRef]
16. Shiri, S.; Yazdani, M.; Pourgol-Mohammad, M. A fatigue damage accumulation model based on stiffness degradation of composite materials. *Mater. Des.* **2015**, *88*, 1290–1295. [CrossRef]
17. Miner, M.A. Cumulative damage in fatigue. *J. Appl. Mech.* **1945**, *67*, 159–164.
18. Marco, S.M.; Starkey, W.L. A concept of fatigue damage. *Trans. ASME* **1954**, *76*, 627–632.
19. Henry, D.L. A theory of fatigue damage accumulation in steel. *Trans. ASME* **1955**, *77*, 913–918.
20. Gatts, R.R. Application of a cumulative damage concept to fatigue. *J. Basic Eng. Trans. ASME* **1961**, *83*, 529–540. [CrossRef]

21. Manson, S.S.; Freche, J.C.; Ensign, C.R. *Application of a Double Linear Damage Rule to Cumulative Fatigue*; NASA TN D-3839; NASA: Washington, DC, USA, 1967.

22. Chaboche, J.L.; Lesne, P.M. A non-linear continuous fatigue damage model. *Fatigue Fract. Eng. Mater. Struct.* **1988**, *11*, 1–17. [CrossRef]

23. Manson, S.S.; Halford, G.R. Practical implementation of the double linear damage rule and damage curve approach for treating cumulative fatigue damage. *Int. J. Fract.* **1981**, *17*, 169–192. [CrossRef]

24. Franke, L.; Dierkes, G. A non-linear fatigue damage rule with an exponent based on a crack growth boundary condition. *Int. J. Fatigue* **1999**, *21*, 761–767. [CrossRef]

25. Miller, K.J.; Mohanmed, H.J.; DelosRios, E.R. *The Behaviour of Short Fatigue Cracks*; Mechanical Engineering Publications: London, UK, 1986.

26. Angelova, D.; Akid, R. A note on modelling short fatigue crack behaviour. *Fatigue Fract. Eng. Mater. Struct.* **1998**, *21*, 771–779. [CrossRef]

27. Polák, J.; Liškutíne, P. Nucleation and short crack growth in fatigued polycrystalline copper. *Fatigue Fract. Eng. Mater. Struct.* **1990**, *13*, 119–133. [CrossRef]

28. McClintock, F.A. A criterion for ductile fracture by the growth of holes. *J. Appl. Mech. Trans. Asme* **1968**, *35*, 363–371. [CrossRef]

29. Rice, J.R.; Tracey, D.M. On the ductile enlargement of voids in triaxial stress fifields. *J. Mech. Phys. Solids* **1969**, *17*, 201–217. [CrossRef]

30. McDowell, D.L.; Gall, K.; Horstemeyer, M.F.; Fan, J. Microstructure-Based fatigue modeling of cast a356-t6 alloy. *Eng. Fract. Mech.* **2003**, *70*, 49–80. [CrossRef]

31. Leuders, S.; Thöne, M. On the mechanical behaviour of titanium alloy TiAl6V4 manufactured byselective laser melting: Fatigue resistance and crack growth performance. *Int. J. Fatigue* **2013**, *48*, 300–307. [CrossRef]

32. Hu, Y.N.; Wu, S.C.; Song, Z.; Fu, Y.N.; Yuan, Q.X.; Zhang, L.L. Effect of microstructural features on the failure behavior of hybrid laser welded AA7020. *Fatigue Fract. Eng. Mater.* **2018**, *41*, 2010–2023. [CrossRef]

33. Desmorat, R.; Tertre, A.D.; Gaborit, P. Multiaxial haigh diagrams from incremental two scale damage analysis. *AerospaceLab* **2015**, 1–15.

34. Wan, H.L.; Wang, Q.; Chenxue, J.; Zhang, Z. Multi-Scale damage mechanics method for fatigue life prediction of additive manufacture structures of Ti-6Al-4V. *Mater. Sci. Eng. A* **2016**, *669*, 269–278. [CrossRef]

35. Lemaitre, J.; Chaboche, J.L. *Mechanics of Solid Materials*; Cambridge University Press: Cambridge, UK, 1994.

36. Lemaitre, J.; Desmorat, R. *Engineering Damage Mechanics: Ductile, Creep, Fatigue and Brittle Failures*; Springer Science & Business Media: Cachan, France, 2005.